GDCh Research Article Angewandte International Edition Chemie www.angewandte.org

How to cite: *Angew. Chem. Int. Ed.* **2025**, e18505
doi.org/10.1002/anie.202518505

Supramolecular Chemistry Hot Paper

Chiral Bifacial Non-Fullerene Acceptors with Chirality-Induced Spin Selectivity: A Homochiral Strategy to Improve Organic Solar Cell Performance

Shuang Li, Fumitaka Ishiwari, Shaoxian Li, Yumi Yakiyama, and Akinori Saeki**

Abstract: Asymmetric design has emerged as an effective strategy to enhance the performance of non-fullerene acceptors (NFAs) in organic solar cells (OSCs). Although most asymmetric NFAs focus on lateral (i.e., left–right) asymmetry, out-of-plane anisotropy has remained underexplored, despite its ability to induce both a vertical dipole moment and molecular chirality, thereby potentially enabling functionalities such as chirality-induced spin selectivity (CISS). With this perspective, we develop chiral and bifacial NFAs, (*S*,*S*)-IE4F, and (*R*,*R*)-IE4F, featuring an indacenodithiophene (IDT) core bearing a hydrophilic oligo(ethylene glycol) group and a hydrophobic phenyl group on the bridging sp^3-carbons. Their racemic counterpart (*rac*-IE4F) and a non-bifacial achiral isomer (*meso*-IE4F) are also synthesized as the controls. Compared to *meso*-IE4F, the bifacial isomers exhibit higher solubility, more favorable molecular packing for carrier transport, and larger dipole moments. Notably, neat (*S*,*S*)/(*R*,*R*)-IE4Fs and their bulk heterojunctions with PBDB-T exhibit pronounced CISS effect, with spin polarizations of ~70% and ~50%, respectively. Consequently, OSCs based on homochiral bifacial IE4Fs achieve a power conversion efficiency of 8.17%, three times higher than that of *meso*-IE4F. This study highlights the impact of isomerization in NFAs and provides a new molecular design strategy for homochiral asymmetric NFAs.

Introduction

Organic solar cells (OSCs) have garnered significant attention as a viable solution for sustainable energy production, attributed to their excellent solution processability, lightweight characteristics, and flexibility.[1–4] In this decade, substantial advancements have been made in the power conversion efficiencies (PCEs) of OSCs, reaching 19%–20% in binary[5,6] and ternary[7–11] single-junction devices, as well as tandem devices.[12–14] Despite these improvements, OSCs still lag behind the lead halide perovskite solar cells (~26% PCE).[15–18] The development of innovative materials is therefore key to further enhancing OSC performance. As such, non-fullerene acceptors (NFAs)[19–21] are the premier class of materials that simultaneously satisfy the requirements of a narrow bandgap energy (E_g), optimal energy offset and miscibility with p-type semiconductors, and large electron mobilities. This is in sharp contrast to the conventional soluble fullerenes.[22–24]

Over the past decade, various molecular design strategies have been explored for NFAs, leading to the development of benchmark molecules such as ITIC and Y6.[25–28] However, these state-of-the-art NFAs generally possess laterally and facially symmetric structures. More recently, the asymmetric molecular design has attracted attention to improve the performance of NFAs (Figure 1a).[29–36] For instance, Li et al.[34] introduced an asymmetric small molecule acceptor, Y6-4O (Figure 1a, right), by attaching highly polarized oligo (ethylene glycol) side chains to the one of two pyrrole units of the Y6 core. The oligo (ethylene glycol)-appended Y6-4O displayed a higher dielectric constant ($\varepsilon_r = 5.13$) than Y6 ($\varepsilon_r = 3.36$), which improved exciton dissociation and reduced charge recombination in OSCs. Feng et al.[37,38] synthesized asymmetric NFAs (Figure 1b, IDT-OB) incorporating one alkyl (*n*-octyl) and one aryl (4-hexylphenyl) side chain on the same sp^3-bridged carbons of indacenodithiophene (IDT) core and achieved a high PCE of 9.17% with the IDT-OB-based OSCs. Introducing asymmetric side chains to bridging sp^3 carbon atoms of C_2 symmetrical π-cores such as IDT leads

[*] S. Li, Prof. Dr. F. Ishiwari, Dr. S. Li, Prof. Dr. Y. Yakiyama, Prof. Dr. A. Saeki
Department of Applied Chemistry, Graduate School of Engineering, Osaka University, 2-1 Yamadaoka, Suita, Osaka 565–0871, Japan
E-mail: ishiwari@chem.eng.osaka-u.ac.jp
saeki@chem.eng.osaka-u.ac.jp

Prof. Dr. F. Ishiwari, Prof. Dr. Y. Yakiyama, Prof. Dr. A. Saeki
Innovative Catalysis Science Division, Institute for Open and Transdisciplinary Research Initiatives (ICS-OTRI), Osaka University, 1-1 Yamadaoka, Suita, Osaka 565–0871, Japan

Prof. Dr. F. Ishiwari
Graduate School of Urban Environmental Sciences, Tokyo Metropolitan University, 1-1 Minamiosawa, Hachioji, Tokyo 192–0297, Japan

Prof. Dr. F. Ishiwari, Prof. Dr. Y. Yakiyama
PRESTO, Japan Science and Technology Agency (JST), Kawaguchi, Saitama 332-0012, Japan

Additional supporting information can be found online in the Supporting Information section

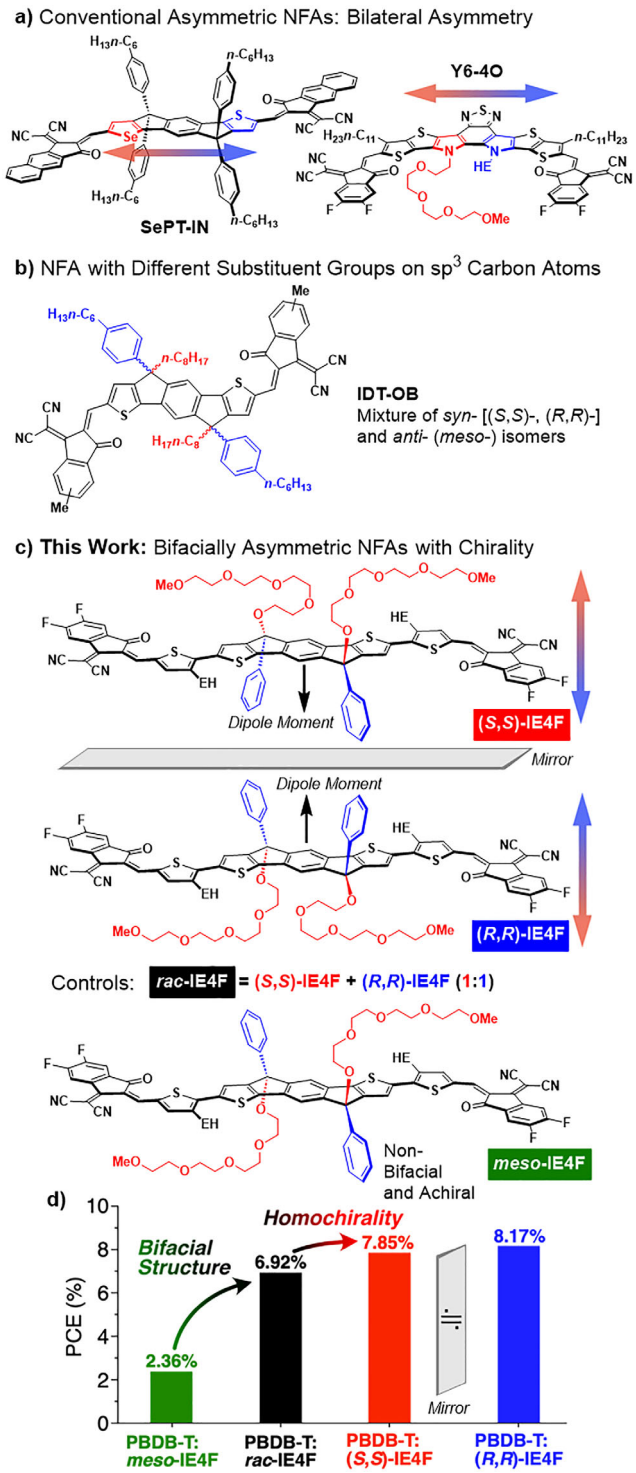

Figure 1. a) Examples of conventional bilateral asymmetric NFAs. b) IDT-based NFA with different substituent groups on sp^3 carbon atoms. c) Molecular structure of bifacially asymmetric and chiral NFA [(*S*,*S*)-IE4F, (*R*,*R*)-IE4F] synthesized in this work. The racemic mixture (*rac*-IE4F) and achiral *meso*-isomer (*meso*-IE4F) were used as controls. EH represents 2-ethylhexyl. d) Summary of PCE values for OSCs of PBDB-T blended with *meso*-, *rac*-, (*S*,*S*)-, and (*R*,*R*)-IE4Fs.

to isomerization and generates NFA molecules as a mixture of *syn* and *anti*-isomers. The *anti*-isomer is centrosymmetric and achiral, while the *syn* isomer is chiral but synthesized as a racemic mixture of (*S*,*S*) and (*R*,*R*) isomers. Accordingly, there has been limited research focusing on the effect of isomerization for OSCs. Indeed, the IDT-OB (Figure 1b) was used as a mixture of *syn* and *anti*-isomers.[37,38] Our group has developed new asymmetric skeletons, namely "bifacial" chiral π-conjugated molecules such as C_2-chiral bifacial indenofluorenes[39,40] and C_3-chiral bifacial truxenes,[41,42] which have two different substituent groups on their bridging sp^3-carbon atoms. These molecules demonstrate efficient surface passivation for perovskite solar cells and circularly polarized luminescence emitters, respectively. Importantly, we have recently reported a C_2-chiral bifacial IDT according to the "bifacial" strategy with application to polymerizing with benzothiadiazole (BT) monomers.[43] The obtained chiral bifacial IDT-BT copolymers exhibit a chirality-induced spin selectivity (CISS) effect with a spin polarization (SP) value of nearly 70% using spin-coated amorphous thin films.[43]

In this work, we proposed and synthesized a series of novel asymmetric NFA molecules named (*S*,*S*)-IE4F, (*R*,*R*)-IE4F (Figure 1c) based on a bifacial IDT π-conjugated backbone to investigate the effects of isomerization in OSCs. The achiral and non-bifacial *anti* isomer (*meso*-IE4F) and the racemic mixture (*rac*-IE4F) of (*S*,*S*)-IE4F, (*R*,*R*)-IE4F were also synthesized and evaluated for comparison. We adopted the π-conjugated core structure of IE4F[44] developed by Z. Ge, J. Hou, and coworkers, due to its facile synthetic procedure. The side-chain design employed the same combination of hydrophilic oligo(ethylene glycol) and hydrophobic phenyl groups as in our previous work.[43] This combination facilitates chiral resolution by chiral HPLC and is also expected to enhance the dipole moment through the contribution of the oligo(ethylene glycol) unit. Compared to non-bifacial *meso*-IE4F, the bifacial NFA molecules [(*S*,*S*)-IE4F, (*R*,*R*)-IE4F, and *rac*-IE4F] exhibit higher dipole moment, enhanced solubility, and more favorable orientation of molecular packing. Interestingly, the spin-coated films of (*S*,*S*)-IE4F and (*R*,*R*)-IE4F exhibited a CISS response with spin polarization values of 60%–70%, similar to our previously reported bifacial IDT-BT polymers. When the bifacial NFAs are integrated with the optically inactive PBDB-T donor polymer, the resulting bulk heterojunctions (BHJs) OSCs demonstrate improved film morphology, efficient charge separation, improved charge transport, and prolonged charge carrier lifetime. Furthermore, the BHJs of PBDB-T:(*S*,*S*)-IE4F and PBDB-T:(*R*,*R*)-IE4F exhibit CISS behavior with the SP values of –48.8 ± 9.3% and + 51.6 ± 10.3%, respectively. To the best of our knowledge, this is the first report on the CISS behavior of OSCs BHJs. These enhancements contribute to higher short-circuit current density (J_{SC}), open-circuit voltage (V_{OC}), and fill factor (FF) values in bifacial NFA-based OSCs. Specifically, the OSC fabricated with PBDB-T:(*S*,*S*)-IE4F and PBDB-T:(*R*,*R*)-IE4F achieved a maximum PCE of ~8%, which is over three times greater than that of PBDB-T:*meso*-IE4F based OSCs (Figure 1d), thereby demonstrating the potential of NFA homochiralization as a new strategy for improving device performance.

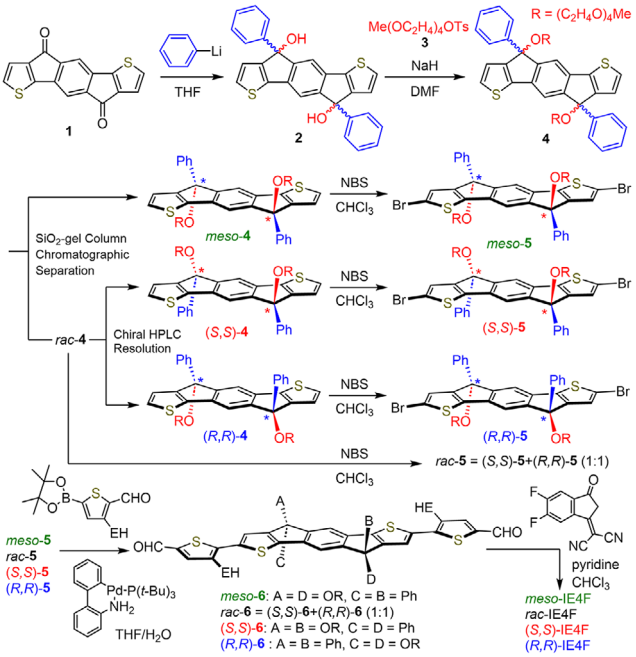

Scheme 1. Synthesis of (*S*,*S*)-IE4F, (*R*,*R*)-IE4F, *rac*-IE4F, and *meso*-IE4F. EH represents 2-ethylhexyl.

Results and Discussion

Synthesis and Theoretical Calculations

According to Scheme 1, *meso*-IE4F, *rac*-IE4F, (*S*,*S*)-IE4F, and (*R*,*R*)-IE4F (Figure 1c) were synthesized following the same procedure as the previously reported IE4F synthesis,[44] except for the use of stereochemically defined IDT cores bearing different substituents on the sp^3-carbon bridge (compounds **5** s). These compounds **5** s enabled the controlled synthesis of meso, racemic, and enantiopure (*S*,*S*)- and (*R*,*R*)-isomers of NFAs and were identical to those employed in our previous synthesis of chiral bifacial IDT-BT copolymers. In our previous study, the meso isomer was not isolated. In the present work, the meso and racemic compounds were successfully separated by SiO_2 column chromatography, with R_f values (*n*-hexane:CH_2Cl_2 = 4:1) of 0.51 for *meso*-**4** (2.5 g, 43% yield) and 0.32 for *rac*-**4** (1.1 g, 19% yield). Subsequently, *rac*-**4** (900 mg) was readily resolved into (*S*,*S*)-**4** (first fraction, 412 mg, 92%) and (*R*,*R*)-**4** (second fraction, 449 mg, 99%) by chiral HPLC (DAICEL, CHIRALPAK IG, diameter: 20 cm × length: 25 cm, eluent: EtOAc : *n*-hexane = 1 : 2).[43] The chemical structure of *meso*-**4** was unambiguously identified by a combination of ^1H and ^{13}C NMR spectroscopy, IR, high-resolution mass spectrometry. Single-crystal X-ray diffraction analysis of *meso*-**5** (Figure S1) clearly determined its meso stereochemistry. The enantiomeric structures of (*S*,*S*)-IE4F and (*R*,*R*)-IE4F were confirmed by their mirror-image circular dichroism (CD) spectra in tetrahydrofuran (THF) (Figure 2a). Thermogravimetric analysis (TGA) revealed a 5% mass loss at over 270 °C for all the obtained IE4Fs (Figure S2), indicating their sufficient thermal stability for OPV application. From the

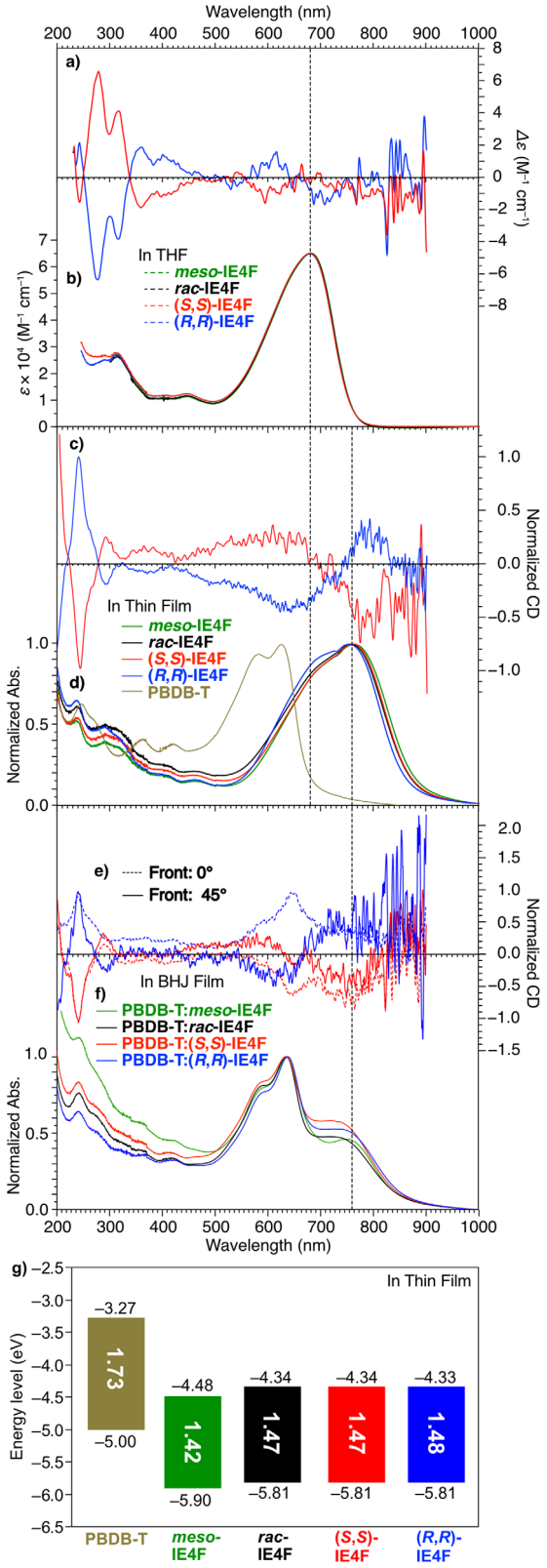

Figure 2. a, c, e) UV–vis absorption and b, d, f) CD spectra of *meso*-IE4F, *rac*-IE4F, (*S*,*S*)-IE4F, and (*R*,*R*)-IE4F a, b) in THF (15 μM), c, d) in thin film states, and e, f) in their BHJ film states with PBDB-T. g) Energy diagram of PBDB-T, *meso*-IE4F, *rac*-IE4F, (*S*,*S*)-IE4F, and (*R*,*R*)-IE4F.

Table 1: Summary of the optical and electronic properties of *meso*-IE4F, *rac*-IE4F, (*S*,*S*)-IE4F, and (*R*,*R*)-IE4F NFA molecules.

	HOMO (eV)]	E_g^{opt} (eV)	LUMO (eV)	λ_{max} (nm)[a]	λ_{max} (nm)[b]	μ (Debye)[c]
meso-IE4F	−5.90	1.42	−4.48	682	763	0
rac-IE4F	−5.81	1.47	−4.34	681	758	–
(*S*,*S*)-IE4F	−5.81	1.47	−4.34	679	760	1.7
(*R*,*R*)-IE4F	−5.81	1.48	−4.33	680	752	1.7

[a] Photoabsorption maximum in THF [b] Photoabsorption maximum in the thin film states [c] Calculated dipole moment.

differential scanning calorimetry (DSC) measurement, these NFAs do not show any clear sign of phase transition in the temperature range of –50–200 °C (Figure S3).

A large dipole moment plays an important role in OSC device performance, because it often leads to a high relative dielectric constant, which in turn can reduce the exciton binding energy and suppress charge recombination losses through stronger intermolecular interactions.[45,46] To evaluate the electron distribution and dipole moments of the IE4Fs molecules, density functional theory (DFT) calculations were performed to compute the electrostatic potential (ESP) and polarization of the molecules, at the B3LYP/6–31G(d,p) level of theory. The calculated dipole moment vectors for (*S*,*S*)-IE4F and (*R*,*R*)-IE4F have magnitudes of 1.7 Debye (Table 1) and are oriented in the out-of-plane direction, pointing from the ether (OR) substituent toward the phenyl (Ph) group (Figures 1c and S4), whereas the magnitude of the dipole moment of *meso*-IE4F is 0 Debye due to its centrosymmetric molecular structure. This value (1.7 D) is comparable to that of previously reported bilaterally asymmetric NFAs, such as Y6-4O (2.6 D),[34] although the former is oriented in the out-of-plane direction. In contrast to previously reported asymmetric NFA designs—which typically induce in-plane dipole moments through lateral structural asymmetry—our bifacial approach enables the introduction of out-of-plane dipole moments via a bifacially asymmetric structure. This result is consistent with the higher molecular polarity of *rac*-IE4F [a 1:1 mixture of (*S*,*S*)-IE4F and (*R*,*R*)-IE4F], which exhibits a lower SiO_2 TLC R_f value of 0.25 (EtOAc:*n*-hexane = 2:3) than *meso*-IE4F (0.60) due to its dipolar bifacial structure. Recent studies have suggested that the magnitude of the quadrupole tensor can play a beneficial role in charge separation processes.[47,48] The quadrupole tensor components of (*S*,*S*)-IE4F were calculated to be XX = –210.083, YY = 101.835, ZZ = 108.248, XY = 75.396, XZ = –0.026, and YZ = 0.009 in the Debye-Å unit.[47] For the (*R*,*R*)-IE4F enantiomer, only the signs of the XY and XZ components are reversed, while YZ and the diagonal components remain unchanged (XX = –210.083, YY = 101.835, ZZ = 108.248, XY = –75.396, XZ = 0.026, and YZ = 0.009). This behavior corresponds to a reflection through the YZ plane (x → –x), which is consistent with the mirror-image relationship between the two molecular structures. The quadrupole tensor magnitudes (Q) calculated for (*S*,*S*)-IE4F and (*R*,*R*)-IE4F were both 147 ea_0^2 (e: elementary of a charge, a_0: Bohr radius). On the other hand, *meso*-IE4F exhibited quadrupole tensor components of XX = –210.395, YY = 102.804, ZZ = 107.590, XY = 74.9, XZ = –7.611, and YZ = 6.542. The Q value calculated from these values was 147 ea_0^2, which is identical to those of (*S*,*S*)-IE4F and (*R*,*R*)-IE4F. This value (147 ea_0^2) is larger than that of a typical NFA such as ITIC (51.3 ea_0^2),[48] which may contribute to efficient charge separation.

Photophysical and Chiroptical Properties

We measured and compared UV–vis absorption and circular CD spectra of IE4Fs in diluted THF solution and in thin films prepared by spin-coating of the chlorobenzene (CB) solution (1500 rpm, 10 mg mL^{-1}) (Figure 2a–f). All the IE4Fs exhibited almost identical UV–vis absorption spectra with the maximum at 680 nm in solution (Figure 2b). A red shift of ~80 nm was observed in the neat IE4F films (Figure 2d) compared to their solution-state spectra, indicating enhanced aggregation or planarization upon film formation. The highest occupied molecular orbital (HOMO) energy levels of the thin films of *meso*-IE4F, *rac*-IE4F, (*S*,*S*)-IE4F, and (*R*,*R*)-IE4F were determined by photoelectron yield spectroscopy (PYS) (Figure S5). Their bandgap energies (E_g) were determined from the onset of UV–vis absorption spectra in the film states (Figure S6), and the lowest unoccupied molecular orbital (LUMO) energy levels were calculated by HOMO + E_g. The energy diagrams of IE4F are summarized in Figure 2g and Table 1. We found that the racemic and homochiral bifacial IE4Fs have similar energy diagrams, whereas the non-bifacial *meso*-IE4F exhibits a slightly lower HOMO level than other bifacial IE4Fs, likely due to the differences in the molecular packing in the thin-film state. The energy diagram of PBDB-T, a representative donor polymer used in the present study, is also shown in Figure 2g. All the IE4Fs have complementary absorption profile and enough HOMO-HOMO and LUMO-LUMO offsets with PBDB-T.

(*S*,*S*) and (*R*,*R*)-IE4F showed mirror-imaged CD spectra in both solution (Figure 2a) and in film (Figure 2c). However, the spectral shapes were markedly different between the two states, as also seen in the absorption spectra (Figure 2b,d), suggesting substantial changes in chiral molecular conformation and higher-order structure upon film formation. The formation of higher-order structure in the film is further supported by the angle- and side-dependent CD responses observed in the film state (Figure S7),[49] as well as by the 2D-GIWAXS measurements discussed in a later section. Notably, the spectral shapes of CD spectra in the film state exhibited clear bisignate CD signals on mainchain charge transfer (CT) band in the longer wavelength region.

We then fabricated BHJ films of the IE4Fs with PBDB-T by spin-coating CB solutions of their 1:1 (w/w) mixtures

(3 mg mL^{-1}) at 2000 rpm on quartz, and measured their UV–vis absorption and CD spectra (Figure 2e,f). The BHJ films of *rac*-, (*S*,*S*)-, and (*R*,*R*)-IE4F with PBDB-T showed slight blue shifts (14.5 nm) in the IE4F absorption bands compared to their neat films. In contrast, the PBDB-T:*meso*-IE4F film showed no such shift, maintaining the same absorption maximum as the neat *meso*-IE4F film. Although the absorption maximum of PBDB-T remained essentially unchanged across all samples, minor changes were observed in the relative intensities of the 0–0 and 0–1 transitions. The CD spectra of BHJ films based on homochiral (*S*,*S*)-IE4F and (*R*,*R*)-IE4F (Figure 2e) exhibited a pronounced dependence on the incident side and angle of the probe light, particularly in the 500–700 nm region corresponding to PBDB-T absorption, and similar behavior was observed for neat PBDB-T films, which are optically inactive (Figure S8). These signals are attributed to artifacts arising from linear dichroism (LD), which strongly depends on the incident angle and measurement side of the probe light (Figure S8).[49] The observed LD likely originates from anisotropic molecular alignment of PBDB-T in the film (as discussed in a later section). In the shorter wavelength region around 250 nm, the BHJ films exhibited CD signals identical to those of the neat (*S*,*S*)-IE4F and (*R*,*R*)-IE4F films (Figure 2c,e). Furthermore, at incident angles where the PBDB-T CD signal was negligible (front: 45°, Figure S7b), the CD spectra of the BHJ films closely matched those of the neat (*S*,*S*)-IE4F and (*R*,*R*)-IE4F films (Figure 2e, solid lines). The preservation of the homochiral NFA-derived chiroptical response in the BHJ films suggests that these systems could also exhibit chirality-induced phenomena such as the CISS effect.

CISS Properties of Neat and BHJ Films

CISS is a phenomenon in which up or down spin-polarized current preferentially passes through a chiral substance to generate spin-polarized current. The CISS effect has attracted much attention because it offers a new approach for manipulating spins.[50,51] Previously, homochiral Y6 derivatives were reported to exhibit CISS effects, which contributed to suppressed charge recombination and enhanced photocatalytic hydrogen evolution performance.[52] However, to date, no study has applied CISS-active homochiral NFAs to OSCs, leaving the impact of molecular chirality on photovoltaic performance largely unexplored. Therefore, we investigated the CISS properties of chiral bifacial NFAs and explored their application in OSCs. The CISS properties of chiral bifacial IE4Fs were evaluated using the same experimental protocol as in our previous study on chiral bifacial IDT-based polymers. (*S*,*S*)-IE4F and (*R*,*R*)-IE4F thin films were fabricated by spin coating their 5 mg mL^{-1} solution in CB at 1500 rpm onto highly oriented pyrolytic graphite (HOPG). The film morphology of (*S*,*S*)-IE4F and (*R*,*R*)-IE4F thin films on HOPG were first characterized by tapping mode atomic force microscope (AFM) as shown in Figure S9. We confirmed the film thickness is 22.6 ± 5.1 nm with root-mean-square surface roughness (R_a) of 0.29 nm for (*S*,*S*)-IE4F neat film and the

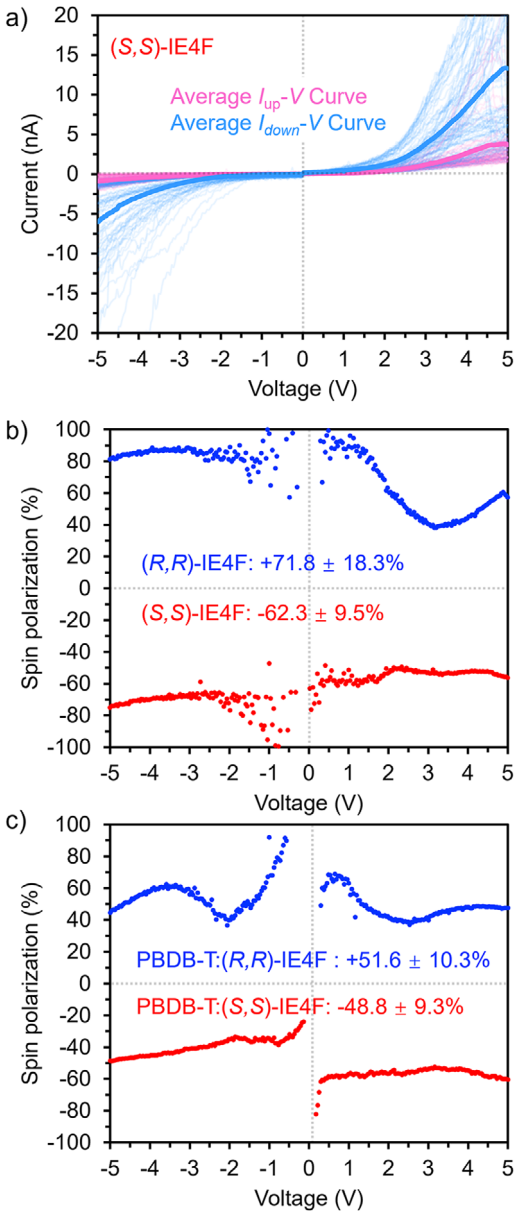

Figure 3. a) Up (pink) or down (sky blue) spin-polarized current–voltage curves of the thin film of (*S*,*S*)-IE4F on HOPG. Unaveraged curves are shown as thin pink and blue lines. Spin polarization as a function of the applied voltage for b) (*S*,*S*)-IE4F (red) and (*R*,*R*)-IE4F (blue) and c) PBDB-T:(*S*,*S*)-IE4F (red) and PBDB-T:(*R*,*R*)-IE4F (blue).

film thickness is 21.8 ± 1.9 nm with R_a of 0.31 nm for (*R*,*R*)-IE4F neat film. A neodymium (Nd) magnet was placed on top of the paramagnetic CoCr cantilever during the measurement, with either the "N" or "S" pole facing the cantilever to maintain its magnetization in the "up" or "down" direction, respectively. This magnetization control allowed for the selective detection of up- and down-spin-polarized currents (I_{up} and I_{down}) throughout the measurement process. To obtain averaged I_{up}-*V* and I_{down}-V characteristics, over 100 *I*-*V* curves were recorded at different sample positions under each magnetization conditions. As a result, the (*S*,*S*)-IE4F thin film exhibit higher I_{down} than I_{up} (Figure 3a), indicating

that down-spin polarized current preferentially passes through the (*S*,*S*)-IE4F thin film. Conversely, the (*R*,*R*)-IE4F thin films exhibited I_{up} than I_{down} (Figure S10), indicating selective transport of up-spin polarized current. These results confirm the observation of the CISS effect in the thin films of the chiral bifacial NFAs. Based on the averaged I_{down}-V and I_{up}-V curves, the spin polarization (SP) values were calculated to be –62.3 ± 9.5% and + 71.8 ± 18.3% (Figure 3b) for (*S*,*S*)-IE4F and (*R*,*R*)-IE4F thin films, respectively. Notably, the chirality-dependent sign of the SP –negative for the (*S*,*S*)-isomer and positive for the (*R*,*R*)-isomer– was consistent with the enantiomer-specific SP behavior previously observed in our bifacial IDT-BT polymers.[43]

For CISS characterization, BHJ films of PBDB-T:(*S*,*S*)-IE4F and PBDB-T:(*R*,*R*)-IE4F were spin-coated onto HOPG from CB solutions (3 mg mL^{-1}, 1:1 w/w) at 2000 rpm, using the same conditions as for the CD measurements. The film thickness was determined to be 22.1 ± 2.5 nm with R_a of 1.17 nm for the (*S*,*S*)-based BHJ film, and 29.8 ± 3.3 nm with R_a of 1.11 nm for the (*R*,*R*)-based film (Figure S9). The resulting BHJ films on HOPG were then evaluated for their CISS properties using the same spin-polarized mc-AFM technique as applied to the neat films. As a result, CISS effect was also observed for these BHJ films (Figure S11), and the SP values of PBDB-T:(*S*,*S*)-IE4F and PBDB-T:(*R*,*R*)-IE4F BHJ films were calculated to be –48.8 ± 9.3% and + 51.6 ± 10.3% (Figure 3c), respectively. These BHJ films exhibited spin selectivity consistent with their neat counterparts: the (*S*,*S*)-based BHJ facilitated preferential transport of down-spin-polarized current, while the (*R*,*R*)-based BHJ favored up-spin-polarized current. Although the observed SP values were slightly lower than those of the neat films, likely due to dilution of the chiral environment by the optically inactive PBDB-T, this result provides the first experimental insight into the CISS behavior of BHJ films composed of homochiral acceptors and optically inactive donors.

Stereochemistry-Dependent Solubility

During the preparation of precursor solutions for spin-coating, we noticed a pronounced difference in solubility among the IE4F isomers depending on their stereochemistry. Accordingly, we examined their solubilities in CB at 25 °C by carefully diluting their saturated solutions (Figure S12). Consequently, the solubilities of *meso*-IE4F in CB at 25 °C was determined to be 6.3 mg mL^{-1}, whereas those of *rac*-IE4F, (*S*,*S*)-IE4F, and (*R*,*R*)-IE4F were approximately 30 mg mL^{-1}, respectively. Despite the different stereochemistries, the bifacial isomers exhibited nearly fivefold higher solubility than the meso isomer, highlighting the significant impact of the bifacial architecture on solubility enhancement. Since a high solubility plays a key role in achieving optimal BHJ nanostructure, these findings underscore the advantages of the bifacial molecular design. Furthermore, the remarked solubility differences among the isomers indicate that stereochemical tuning can serve as an effective strategy for improving solubility in chiral π-conjugated systems.

Photovoltaic Performance

To investigate photovoltaic performance, a series of OSC devices based on PBDB-T:IE4Fs were fabricated with an inverted structure of glass/ITO/ZnO/BHJ/MoO_3/Ag, which is described in detail in Supporting Information. The film thicknesses of the active layers of PBDB-T:*meso*-IE4F, PBDB-T:*rac*-IE4F, PBDB-T:(*S*,*S*)-IE4F, and PBDB-T:(*R*,*R*)-IE4F blends under the optimized conditions were measured to be 131, 99, 101, and 106 nm, respectively. The current density–voltage (*J*–*V*) curves of the best performing OSCs measured under simulated AM 1.5 G solar simulator illumination are shown in Figure 4a, and the corresponding photovoltaic parameters are summarized in Table 2. The *rac*-IE4F, (*S*,*S*)-IE4F, and (*R*,*R*)-IE4F-based OSCs exhibited overall superior J_{SC}, V_{OC}, and FF values compared to *meso*-IE4F-based OSCs. Consequently, the best performing OSCs based on *rac*-IE4F, (*S*,*S*)-IE4F, and (*R*,*R*)-IE4F exhibited PCE of 6.92%, 7.85%, and 8.17%, respectively, which is over three times greater than 2.36% of *meso*-IE4F-based OSC. Notably, owing to larger J_{SC} and FF values, the enantiomerically pure (*S*,*S*)-IE4F and (*R*,*R*)-IE4F-based OSCs exhibited further higher PCE compared to *rac*-IE4F-based OSCs. The external quantum efficiency (EQE) spectra (Figure 4b) revealed maximum EQE values of 63%, 67%, and 65% for *rac*-, (*S*,*S*)- and (*R*,*R*)-IE4F-based devices, respectively, while the *meso*-IE4F-based devices exhibited a much lower value of 28%. Importantly, despite the nearly identical absorption spectra of the BHJ films (Figure 2f), the J_{SC} integrated from EQE curves also supported the measured J_{SC} (Table 2).

To understand the charge recombination mechanism of the OSC devices, the dependence of J_{SC} under different light intensities (P_{light}) was measured (Figure 4c). The correlation between J_{SC} and P_{light} can be represented as $J_{SC} \propto P_{light}^{S}$. When the slope of the logarithmic plot (*S*) is close to 1, the bimolecular charge recombination in the device is negligible. The *S* values were determined to be 0.959, 0.966, 0.982, and 0.985 for *meso*-IE4F, *rac*-IE4F, (*S*,*S*)-IE4F, and (*R*,*R*)-IE4F-based OSCs, respectively. Compared to *rac*-IE4F-based OSCs, the weaker bimolecular recombination in (*S*,*S*)-IE4F and (*R*,*R*)-IE4F-based OSCs is responsible for the enhancement of J_{SC} and FF. Li et al. have recently reported that in homochiral Y6-based systems exhibiting the CISS effect, spin-selective charge transport may contribute to the suppression of charge recombination.[52] Although the underlying mechanism remains under investigation, it is noteworthy that our (*S*,*S*)- and (*R*,*R*)-IE4F-based OSCs, which exhibit CISS, show reduced bimolecular recombination, potentially hinting at a related phenomenon. The *meso*-IE4F-based OSC showed a slightly small but almost comparable *S* value of 0.959. Accordingly, the low J_{SC} of *meso*-IE4F-based OSC could be attributed to the low charge separation efficiency influenced by phase separation in the BHJ film (vide infra).

Furthermore, to evaluate the charge extraction in the devices, we investigated the relationship between photocurrent density (J_{ph}, defined as $J_L - J_D$, where J_L and J_D are the current densities under illumination and in dark, respectively) and the effective voltage (V_{eff}, defined as $V_0 - V$, where V is the applied voltage and V_0 is the voltage at when

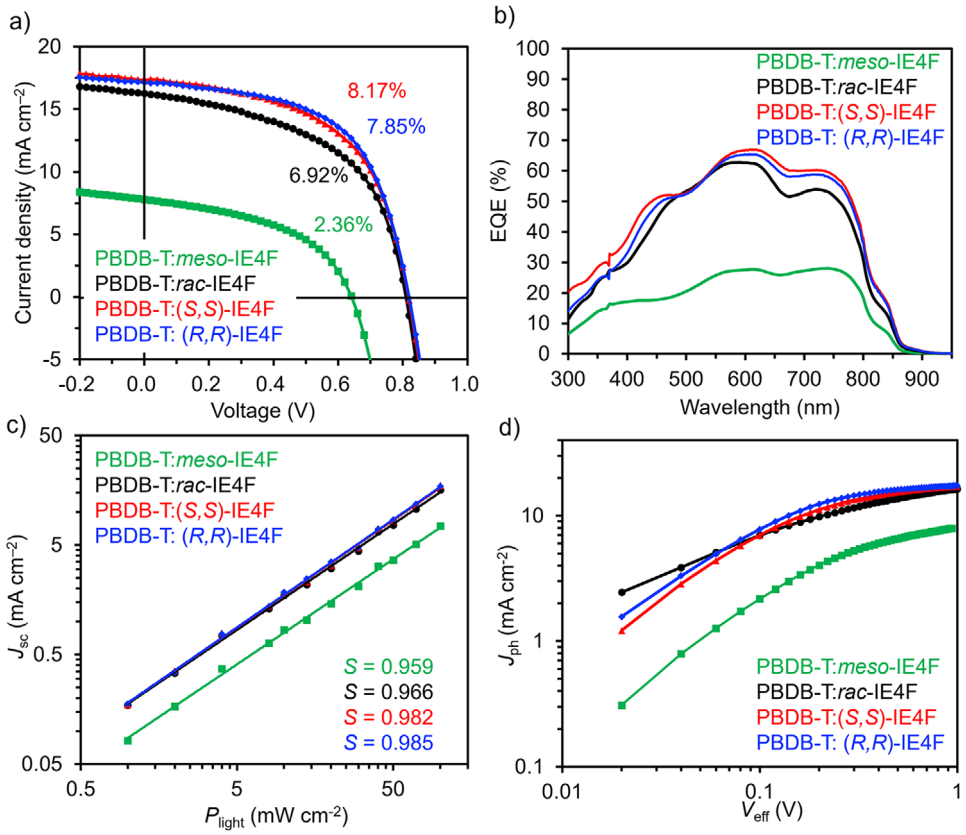

Figure 4. a) J—V curves and b) corresponding EQE spectra of best-performing OSCs devices. c) Light intensity dependence of J_{sc} and d) J_{ph} versus V_{eff}. The PCE and slope are appended in (a) and (c), respectively.

Table 2: Photovoltaic parameters of OSCs under pseudo sunlight at 100 mW cm^{-2}.[a)]

Active layers	J_{SC} (mA cm^{-2})	J_{SC}^{EQE} (mA cm^{-2})	V_{OC} (V)	FF (%)	PCE (%)
PBDB-T:*meso*-IE4F	7.802 (7.47 ± 0.27)	7.02	0.641 (0.586 ± 0.082)	47.2 (41.4 ± 5.4)	2.36 (1.84 ± 0.44)
PBDB-T:*rac*-IE4F	16.25 (15.93 ± 0.35)	14.86	0.810 (0.780 ± 0.028)	52.6 (47.9 ± 3.3)	6.92 (5.95 ± 0.50)
PBDB-T:(*S*,*S*)-IE4F	17.35 (16.80 ± 0.55)	16.23	0.820 (0.789 ± 0.022)	55.3 (51.8 ± 4.0)	7.85 (6.88 ± 0.73)
PBDB-T:(*R*,*R*)-IE4F	17.12 (16.56 ± 0.76)	15.70	0.820 (0.798 ± 0.011)	58.2 (51.8 ± 5.0)	8.17 (6.85 ± 0.90)

[a)] ITO/ZnO/BHJ/MoO_x/Ag. Blend ratio is D:A = 1:1 in CB with 0.5vol% 1,8-diiodooctane (DIO). The values in the brackets are the averages calculated from more than 10 devices, while others are the parameters of maximum-PCE devices.

J_{ph} is zero), as shown in Figure 4d. The charge extraction probability (P_{ext}) was calculated as the ratio of photocurrent density (J_{ph}) to the saturated photocurrent density (J_{sat}), where J_{ph} under the short-circuit conditions. The P_{ext} values of PBDB-T:*meso*-IE4F, PBDB-T:*rac*-IE4F, PBDB-T:(*S*,*S*)-IE4F, and PBDB-T:(*R*,*R*)-IE4F based-OSCs were calculated to be 93.7%, 95.9%, 98.1%, and 97.7%, respectively. It also supports the result that enantiomerically pure (*S*,*S*)-IE4F and (*R*,*R*)-IE4F based-OSCs performed the highest J_{SC}.

Structural Analysis of Neat and BHJ Films

Two-dimensional grazing incidence wide-angle X-ray scattering (2D-GIWAXS) was conducted on the neat (IE4Fs) and blended films (PBDB-T:IE4Fs). The 2D-GIWAXS images and the corresponding out-of-plane (OOP) and in-plane (IP) 1D profiles are shown in Figures 5 and S13, respectively. Among the neat films, *meso*-IE4F exhibited a markedly different 2D-GIWAXS pattern (Figure 5a) compared to the other isomers (Figure 5b–d). The *meso*-IE4F film (Figure 5a) showed a dominant diffraction peak in the IP direction at $q_{xy} \approx 18.2$ nm^{-1} ($d \approx 3.45$ Å), corresponding to π–π stacking, along with a prominent lamellar stacking peak in the OOP direction ($q_z \approx 3.9$ nm^{-1}, $d \approx 16.3$ Å), suggesting an edge-on orientation. Notably, additional spot diffractions were observed along off-axis directions in the 2D-GIWAXS image of *meso*-IE4F (white arrows), suggesting the presence of a 3D molecular ordering unique to this stereoisomer. In contrast, the *rac*-, (*S*,*S*)-, and (*R*,*R*)-IE4F films (Figure 5b–d) exhibited strong π–π stacking diffraction predominantly in the OOP direction ($q_z \approx 18.3$–18.4 nm^{-1}), indicative of a face-on

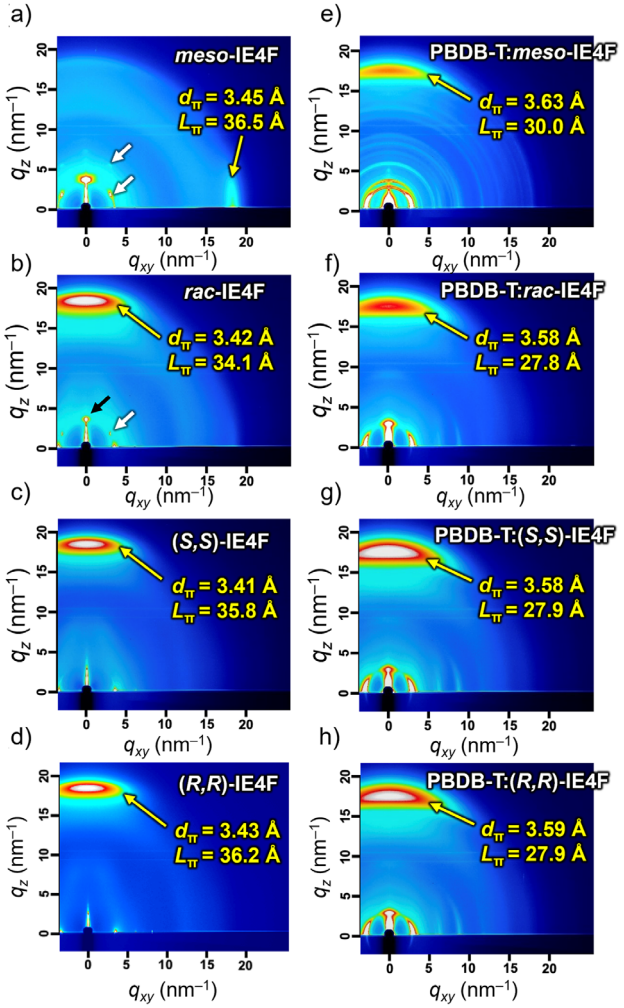

Figure 5. 2D-GIWAXS images of a) *meso*-IE4F, b) *rac*-IE4F, c) (*S*,*S*)-IE4F, and d) (*R*,*R*)-IE4F neat films. Those of BHJ blend films are shown in e–h), respectively. The *d*-spacing (d_π) and its coherence length (L_π) are superimposed. 1D profiles along in-plane and out-of-plane directions are shown in Figure S13.

orientation favorable for vertical charge transport. However, a closer inspection of the 2D-GIWAXS patterns reveals subtle yet distinct differences between *rac*-IE4F and the enantiopure (*S*,*S*)- and (*R*,*R*)-IE4F films, as detailed below. Specifically, the *rac*-IE4F film (Figure 5b) exhibits a prominent diffraction peak in the OOP direction at $q_z \approx 3.9$ nm^{-1} (black arrows in Figures 5b and S13) in addition to off-axis spot diffraction (white arrow), indicating the presence of a much higher-order 3D molecular ordering. In contrast, such diffraction features are absent in the enantiopure (*S*,*S*)- and (*R*,*R*)-IE4F films, suggesting that the racemic film adopts a more ordered supramolecular structure than its enantiopure counterparts. It is also noteworthy that the enantiopure (*S*,*S*)-IE4F and (*R*,*R*)-IE4F neat films (Figure 5c,d) exhibited crystal coherence lengths (L_π) of 35.8 and 36.2 Å, respectively, which are larger than the 34.1 Å observed for *rac*-IE4F (Figure 5b).

In the 2D-GIWAXS pattern of the PBDB-T:*meso*-IE4F blend film (Figure 5e), a diffraction peak at $q_z \approx 17.3$ nm^{-1}, characteristic of the face-on π–π stacking of PBDB-T, was

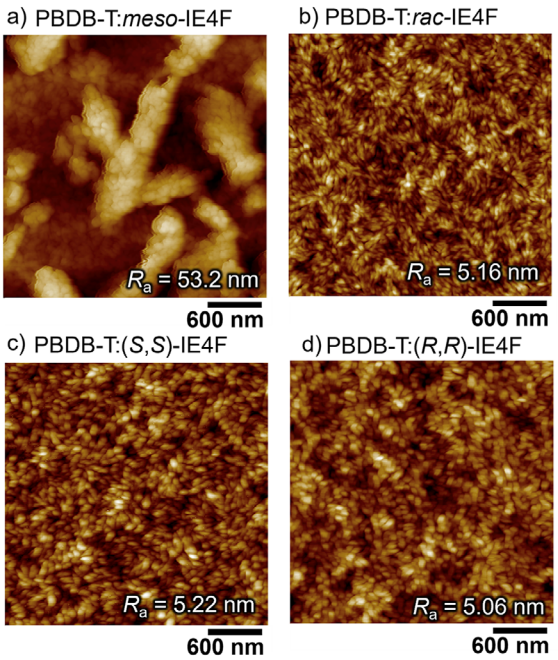

Figure 6. AFM height images of a) PBDB-T:*meso*-IE4F, b) PBDB-T:*rac*-IE4F, c) PBDB-T:(*S*,*S*)-IE4F, and d) PBDB-T:(*R*,*R*)-IE4F blend films. The R_a values are superimposed. The image size is 3 × 3 μm^2, and the color scale is 0–330 nm for (a) and 0–40 nm for (b–d).

observed. In addition, multiple isotropic Debye–Scherrer rings derived from *meso*-IE4F were observed, indicating the presence of randomly oriented microcrystalline domains of *meso*-IE4F. These features suggest that PBDB-T and *meso*-IE4F crystallized separately due to their poor miscibility, leading to a disordered and non-uniform blend microstructure. In contrast, the PBDB-T:*rac*-IE4F, PBDB-T:(*S*,*S*)-IE4F, and PBDB-T:(*R*,*R*)-IE4F blend films (Figure 5f–h) showed stronger face-on-orientated diffraction than the PBDB-T:*meso*-IE4F film. This can be attributed to the overlapping face-on π–π stacking contributions from both PBDB-T and the bifacial IE4Fs. This preferred orientation is beneficial for vertical charge transport in OSC devices. Overall, the 2D-GIWAXS analyses of both neat and BHJ films reveal that the bifacial NFA design promotes more ordered π–π stacking in the out-of-plane direction and facilitates favorable molecular alignment, particularly in the enantiopure systems, thereby supporting more efficient charge extraction and higher photovoltaic performance.

We also investigated the surface structure of BHJ films by AFM, and the corresponding topography images are shown in Figure 6. AFM observation of PBDB-T:*meso*-IE4F BHJ (Figure 6a) revealed a non-uniform surface with large aggregates of *meso*-IE4F molecules, consistent with multiple Debye–Scherrer rings in the GIWAXS measurements. The R_a of the PBDB-T:*meso*-IE4F BHJ film was 53.2 nm (Figure 6a). The rough texture of the film quality was also observed by optical microscope (Figure S14). In contrast, the PBDB-T:*rac*-IE4F, PBDB-T:(*S*,*S*)-IE4F and PBDB-T:(*R*,*R*)-IE4F blend films exhibited interpenetrating networks with nanoscale phase-separated domains (Figure 6b–d), which is typical of

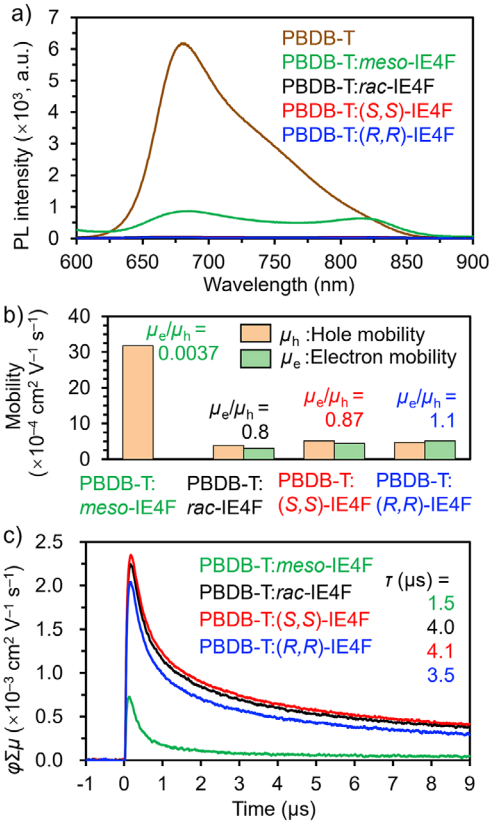

Figure 7. a) PL spectra of PBDB-T and PBDB-T:*meso*-IE4F, PBDB-T:*rac*-IE4F, PBDB-T:(*S*,*S*)-IE4F, and PBDB-T:(*R*,*R*)-IE4F blend films excited at 550 nm. b) Comparison of electron and hole mobility values of PBDB-T:*meso*-IE4F, PBDB-T:*rac*-IE4F, PBDB-T:(*S*,*S*)-IE4F, and PBDB-T:(*R*,*R*)-IE4F blend films. c) TRMC profiles of the blend films excited at 500 nm. The average lifetime (τ) obtained by double exponential fitting is appended. The PBDB-T:IE4F blend ratio in these measurements was 1:1 in weight percentage.

optimized BHJ films. The R_a values of the PBDB-T:*rac*-IE4F, PBDB-T:(*S*,*S*)-IE4F, and PBDB-T:(*R*,*R*)-IE4F blend films were 5.16, 5.22, and 5.06 nm, respectively. This favorable morphology facilitates efficient exciton diffusion and dissociation, enhances carrier transport, and suppresses recombination, which is a key factor influencing the device performance.

Exciton and Charge Carrier Dynamics in BHJ Films

To investigate the charge separation efficiency, photoluminescence (PL) measurements under 550 nm excitation were conducted for the PBDB-T, IE4Fs neat films and their blend films (Figure 7a). The PBDBT:*meso*-IE4F blend film exhibited 86% PL quenching of PBDB-T, while the PBDB-T:*rac*-IE4F, PBDB-T:(*S*,*S*)-IE4F, and PBDB-T:(*R*,*R*)-IE4F blend films showed PL quenching as high as 99.3%, 99.3%, and 99.6%, respectively. Compared to PBDBT:*meso*-IE4F blend, PBDB-T:*rac*-IE4F, PBDB-T:(*S*,*S*)-IE4F, and PBDB-T:(*R*,*R*)-IE4F blends exhibited more efficient excitons dissociation into charge carriers, which is consistent with the higher J_{SC} values of these devices relative to the meso-based device.

Furthermore, the Urbach energies (E_u) of the PBDB-T:*meso*-IE4F, PBDB-T:*rac*-IE4F, PBDB-T:(*S*,*S*)-IE4F, and PBDB-T:(*R*,*R*)-IE4F blends were calculated to be 81, 46, 47, and 55 meV (Figure S15), respectively. The higher degree of energetic disorder in the PBDB-T:*meso*-IE4F blend film is consistent with its inferior BHJ film structure and results in more severe energy loss in the OSCs.

The space-charge-limited current (SCLC) method was employed to evaluate the charge carrier mobility of PBDB-T:IE4Fs based OSCs. The hole mobility (μ_h) and electron mobility (μ_e) were obtained by fitting the *J*–*V* curves with the Mott–Gurney law. As a result, the PBDB-T:*meso*-IE4F BHJ exhibited μ_h of 3.2×10^{-3} cm^2 V^{-1} s^{-1} and μ_e of 2.1×10^{-5} cm^2 V^{-1} s^{-1}, leading to a highly unbalanced μ_e/μ_h ratio of 0.0037 (Figures 7b and S16, Table S1). This large imbalance is attributed to the tendency of *meso*-IE4F molecules prefer to form large-scale aggregates rather than being uniformly distributed in the BHJ film, which disrupts continuous electrons transport pathways and results in lower FF and J_{SC} values. On the contrary, PBDB-T:*rac*-IE4F, (*S*,*S*)-IE4F, and (*R*,*R*)-IE4F blend systems more balanced μ_e/μ_h ratios of 0.80, 0.87, and 1.1, respectively, along with reasonable μ_h and μ_e of 3–5 $\times 10^{-4}$ cm^2 V^{-1} s^{-1}. In particular, the enantiopure (*S*,*S*)-IE4F and (*R*,*R*)-IE4F-based BHJs showed not only higher μ_e and μ_h than PBDB-T:*rac*-IE4F blend, but also more balanced charge transport. These characteristics contribute to the higher J_{SC} and FF observed in the PBDB-T:(*S*,*S*)-IE4F and PBDB-T:(*R*,*R*)-IE4F-based OSCs compared to the PBDB-T:*rac*-IE4F-based device.

As an electrode-less method to investigate charge carrier dynamics, time-resolved microwave conductivity (TRMC)[53,54] measurements were performed for the BHJs with various blending weight ratios (Figure S17). Figure 7c shows $\phi\Sigma\mu$ of four PBDB-T:IE4Fs blend films with a 1:1 weight ratio, where $\Sigma\mu$ and ϕ are the sum of the positive and negative charge carrier mobilities, and the charge carrier generation efficiency at the pulse-end, respectively. As a consequence, PBDB-T:*rac*-IE4F, PBDB-T:(*S*,*S*)-IE4F, and PBDB-T:(*R*,*R*)-IE4F BHJ films exhibited $\phi\Sigma\mu_{max}$ of 2.3×10^{-3}, 2.3×10^{-3}, and 2.0×10^{-3} cm^2 V^{-1} s^{-1}, respectively, while the $\phi\Sigma\mu_{max}$ of PBDB-T:*meso*-IE4F BHJ is 7.3×10^{-4} cm^2 V^{-1} s^{-1}. These results are consistent with the observed trends in J_{SC} values of the OSCs, where the *r*ac-IE4F, (*S*,*S*)-IE4F, and (*R*,*R*)-IE4F-based devices outperform the *meso*-IE4F-based one. The charge carrier lifetimes of PBDB-T:*meso*-IE4F, PBDB-T:*rac*-IE4F, PBDB-T:(*S*,*S*)-IE4F, and PBDB-T:(*R*,*R*)-IE4F BHJs were analyzed by fitting TRMC curves using double exponential functions. As shown in Figure 7c, the PBDB-T:*rac*-IE4F, PBDB-T:(*S*,*S*)-IE4F, and PBDB-T:(*R*,*R*)-IE4F BHJs exhibited effective lifetime (τ) of 4.0, 4.1, and 3.5 μs, respectively. In contrast, PBDB-T:*meso*-IE4F BHJ showed the shorter lifetime of 1.5 μs, again indicating its less favorable charge transport characteristics. The consistent trends across device performance and the corresponding electrical, optical, and morphological measurements highlight the advantages of our bifacial NFAs. Interestingly, the enantiopure systems also exhibited pronounced CISS effects, which may provide an additional avenue for enhancing device function.

Conclusion

In this work, we developed a series of novel asymmetric NFA molecules, namely *meso*-IE4F, *rac*-IE4F, (*S*,*S*)-IE4F, and (*R*,*R*)-IE4F, based on an asymmetric IDT backbone with different substituents (i.e., phenyl and ether groups) on its sp^3 carbons. Compared to achiral and centrosymmetric *meso*-IE4F, the chiral and bifacial *rac*-IE4F, (*S*,*S*)-IE4F, and (*R*,*R*)-IE4F NFAs have a large dipole moment, enhanced solubility, and more favorable face-on orientation in the thin film states. When integrated with PBDB-T, the BHJs with *rac*-IE4F, (*S*,*S*)-IE4F, and (*R*,*R*)-IE4F showed good film morphology, efficient charge separation, enhanced charge transport, and long charge carrier lifetimes. We have also revealed that neat films of (*S*,*S*)-IE4F and (*R*,*R*)-IE4F and their BHJs with PBDB-T exhibit CISS with spin polarizations of ~70% and ~50%, respectively. Most importantly, the enantiomerically pure (*S*,*S*)-IE4F and (*R*,*R*)-IE4F-based OSCs exhibited higher PCE than *meso*-IE4F and *rac*-IE4F-based OSCs. Based on these findings, we propose a homochiral strategy to enhance the device performance of OSCs, either through favorable molecular packing that facilitates carrier transport or through recombination suppression enabled by the CISS effect. This study introduces the concepts of molecular chirality and CISS effect, which have not yet been fully explored in the field of organic photovoltaics, and presents a new molecular design strategy for developing high-performance chiral photovoltaic materials. These findings may also open up possibilities for developing new spin photovoltaic devices[55] based on the CISS effect in chiral active layers.

Acknowledgements

The authors acknowledge the financial support received from the Japan Science and Technology Agency (JST) PRESTO (JPMJPR21A2 to F.I.), CREST (JPMJCR23O2 to A.S.) and KAKENHI of the Japan Society for the Promotion of Science (JSPS) (JP23H02013, JP22H04541, JP23H04626, and JP25H01409 to F.I. and JP20H05836 and JP24H00484 to A.S.). The computation was performed using the Research Center for Computational Science, Okazaki, Japan (Projects; 23-IMS-C231, 24-IMS-C278, 25-IMS-C381). The authors are grateful to Dr Tomoyuki Koganezawa at JASRI for his support with the 2D-GIXRD experiments, which were conducted at SPring-8, JASRI, with a proposal number 2023B1758 and 2024B1970. This work was also supported by the Yazaki Memorial Foundation for Science and Technology, the Foundation for the Promotion of Ion Engineering, Kansai Research Foundation for Technology Promotion, and the Research Program of "Five-Star Alliance" in "NJRC Mater. & Den".

Conflict of Interests

The authors declare no conflict of interest.

Data Availability Statement

The data that support the findings of this study are available in the Supporting Information of this article.

Keywords: Chiral bifacial molecules · Chirality-induced spin selectivity · Indacenodithiophene · Non-fullerene acceptor · Organic solar cells

[1] X. Che, Y. Li, Y. Qu, S. R. Forrest, *Nat. Energy* **2018**, *3*, 422–427, https://doi.org/10.1038/s41560-018-0134-z.
[2] T. T. Yan, W. Song, J. M. Huang, R. X. Peng, L. K. Huang, Z. Y. Ge, *Adv. Mater.* **2019**, *31*, 1902210, https://doi.org/10.1002/adma.201902210.
[3] G. Zhang, F. R. Lin, F. Qi, T. Heumüller, A. Distler, H.-J. Egelhaaf, N. Li, P. C. Y. Chow, C. J. Brabec, A. K. Y. Jen, H.-L. Yip, *Chem. Rev.* **2022**, *122*, 14180–14274, https://doi.org/10.1021/acs.chemrev.1c00955.
[4] Y. Zhao, Z. Li, C. Deger, M. Wang, M. Peric, Y. Yin, D. Meng, W. Yang, X. Wang, Q. Xing, B. Chang, E. G. Scott, Y. Zhou, E. Zhang, R. Zheng, J. Bian, Y. Shi, I. Yavuz, K.-H. Wei, K. N. Houk, Y. Yang, *Nat. Sustain.* **2023**, *6*, 539–548, https://doi.org/10.1038/s41893-023-01071-2.
[5] L. Zhu, M. Zhang, J. Xu, C. Li, J. Yan, G. Zhou, W. Zhong, T. Hao, J. Song, X. Xue, Z. Zhou, R. Zeng, H. Zhu, C.-C. Chen, R. C. I. MacKenzie, Y. Zou, J. Nelson, Y. Zhang, Y. Sun, F. Liu, *Nat. Mater.* **2022**, *21*, 656–663, https://doi.org/10.1038/s41563-022-01244-y.
[6] C. Guo, Y. Fu, D. Li, L. Wang, B. Zhou, C. Chen, J. Zhou, Y. Sun, Z. Gan, D. Liu, W. Li, T. Wang, *Adv. Mater.* **2023**, *35*, 2304921, https://doi.org/10.1002/adma.202304921.
[7] T. Chen, S. Li, Y. Li, Z. Chen, H. Wu, Y. Lin, Y. Gao, M. Wang, G. Ding, J. Min, Z. Ma, H. Zhu, L. Zuo, H. Chen, *Adv. Mater.* **2023**, *35*, 2300400, https://doi.org/10.1002/adma.202300400.
[8] H. Chen, S. Y. Jeong, J. Tian, Y. Zhang, D. R. Naphade, M. Alsufyani, W. Zhang, S. Griggs, H. Hu, S. Barlow, H. Y. Woo, S. R. Marder, T. D. Anthopoulos, I. McCulloch, Y. Lin, *Energy Environ. Sci.* **2023**, *16*, 1062–1070, https://doi.org/10.1039/D2EE03483B.
[9] Z. Luo, W. Wei, R. Ma, G. Ran, M. H. Jee, Z. Chen, Y. Li, W. Zhang, H. Y. Woo, C. Yang, *Adv. Mater.* **2024**, *36*, 2407517, https://doi.org/10.1002/adma.202407517.
[10] S. Guan, Y. Li, C. Xu, N. Yin, C. Xu, C. Wang, M. Wang, Y. Xu, Q. Chen, D. Wang, L. Zuo, H. Chen, *Adv. Mater.* **2024**, *36*, 2400342, https://doi.org/10.1002/adma.202400342.
[11] Y. Jiang, S. Sun, R. Xu, F. Liu, X. Miao, G. Ran, K. Liu, Y. Yi, W. Zhang, X. Zhu, *Nat. Energy* **2024**, *9*, 975–986, https://doi.org/10.1038/s41560-024-01557-z.
[12] J. Wang, Z. Zheng, Y. Zu, Y. Wang, X. Liu, S. Zhang, M. Zhang, J. Hou, *Adv. Mater.* **2021**, *33*, 2102787, https://doi.org/10.1002/adma.202102787.
[13] Z. Zheng, J. Wang, P. Bi, J. Ren, Y. Wang, Y. Yang, X. Liu, S. Zhang, J. Hou, *Joule* **2022**, *6*, 171–184, https://doi.org/10.1016/j.joule.2021.12.017.
[14] J. Wang, M. Zhang, J. Lin, Z. Zheng, L. Zhu, P. Bi, H. Liang, X. Guo, J. Wu, Y. Wang, L. Yu, J. Li, J. Lv, X. Liu, F. Liu, J. Hou, Y. Li, *Energy Environ. Sci.* **2022**, *15*, 1585–1593, https://doi.org/10.1039/D1EE03673D.
[15] Y. Zhao, F. Ma, Z. Qu, S. Yu, T. Shen, H.-X. Deng, X. Chu, X. Peng, Y. Yuan, X. Zhang, J. You, *Science* **2022**, *377*, 531–534, https://doi.org/10.1126/science.abp8873.

[16] J. Park, J. Kim, H.-S. Yun, M. J. Paik, E. Noh, H. J. Mun, M. G. Kim, T. J. Shin, S. Il Seok, *Nature* **2023**, *616*, 724–730, https://doi.org/10.1038/s41586-023-05825-y.

[17] Z. Liang, Y. Zhang, H. Xu, W. Chen, B. Liu, J. Zhang, H. Zhang, Z. Wang, D.-H. Kang, J. Zeng, X. Gao, Q. Wang, H. Hu, H. Zhou, X. Cai, X. Tian, P. Reiss, B. Xu, T. Kirchartz, Z. Xiao, S. Dai, N.-G. Park, J. Ye, X. Pan, *Nature* **2023**, *624*, 557–563, https://doi.org/10.1038/s41586-023-06784-0.

[18] R. Azmi, D. S. Utomo, B. Vishal, S. Zhumagali, P. Dally, A. M. Risqi, A. Prasetio, E. Ugur, F. Cao, I. F. Imran, A. A. Said, A. R. Pininti, A. S. Subbiah, E. Aydin, C. Xiao, S. Il Seok, S. De Wolf, *Nature* **2024**, *628*, 93–98, https://doi.org/10.1038/s41586-024-07189-3.

[19] Y. Lin, Z.-G. Zhang, H. Bai, J. Wang, Y. Yao, Y. Li, D. Zhu, X. Zhan, *Energy Environ. Sci.* **2015**, *8*, 610–616, https://doi.org/10.1039/C4EE03424D.

[20] Y. Lin, J. Wang, Z.-G. Zhang, H. Bai, Y. Li, D. Zhu, X. Zhan, *Adv. Mater.* **2015**, *27*, 1170–1174, https://doi.org/10.1002/adma.201404317.

[21] J. Yuan, Y. Zhang, L. Zhou, G. Zhang, H.-L. Yip, T.-K. Lau, X. Lu, C. Zhu, H. Peng, P. A. Johnson, M. Leclerc, Y. Cao, J. Ulanski, Y. Li, Y. Zou, *Joule* **2019**, *3*, 1140–1151, https://doi.org/10.1016/j.joule.2019.01.004.

[22] N. Liang, K. Sun, Z. Zheng, H. Yao, G. Gao, X. Meng, Z. Wang, W. Ma, J. Hou, *Adv. Energy Mater.* **2016**, *6*, 1600060, https://doi.org/10.1002/aenm.201600060.

[23] E. M. Speller, A. J. Clarke, J. Luke, H. K. H. Lee, J. R. Durrant, N. Li, T. Wang, H. C. Wong, J.-S. Kim, W. C. Tsoi, Z. Li, *J. Mater. Chem. A* **2019**, *7*, 23361–23377, https://doi.org/10.1039/C9TA05235F.

[24] X. Du, S. Tao, L. Li, W. Wang, C. Zheng, H. Lin, X. Zhang, X. Zhang, *Sol. RRL* **2018**, *2*, 1800038, https://doi.org/10.1002/solr.201800038.

[25] H. Yao, Y. Chen, Y. Qin, R. Yu, Y. Cui, B. Yang, S. Li, K. Zhang, J. Hou, *Adv. Mater.* **2016**, *28*, 8283–8287, https://doi.org/10.1002/adma.201602642.

[26] H. Yao, Y. Cui, D. Qian, C. S. Ponseca Jr, A. Honarfar, Y. Xu, J. Xin, Z. Chen, L. Hong, B. Gao, R. Yu, Y. Zu, W. Ma, P. Chabera, T. Pullerits, A. Yartsev, F. Gao, J. Hou, *J. Am. Chem. Soc.* **2019**, *141*, 7743–7750, https://doi.org/10.1021/jacs.8b12937.

[27] Y. Cui, H. Yao, J. Zhang, K. Xian, T. Zhang, L. Hong, Y. Wang, Y. Xu, K. Ma, C. An, C. He, Z. Wei, F. Gao, J. Hou, *Adv. Mater.* **2020**, *32*, e1908205, https://doi.org/10.1002/adma.201908205.

[28] C. Li, J. Zhou, J. Song, J. Xu, H. Zhang, X. Zhang, J. Guo, L. Zhu, D. Wei, G. Han, J. Min, Y. Zhang, Z. Xie, Y. Yi, H. Yan, F. Gao, F. Liu, Y. Sun, *Nat. Energy* **2021**, *6*, 605–613, https://doi.org/10.1038/s41560-021-00820-x.

[29] J. Song, Z. Bo, *Chin. Chem. Lett.* **2023**, *34*, 108163, https://doi.org/10.1016/j.cclet.2023.108163.

[30] Y. Zhang, Y. Ji, Y. Zhang, W. Zhang, H. Bai, M. Du, H. Wu, Q. Guo, E. Zhou, *Adv. Funct. Mater.* **2022**, *32*, 2205115, https://doi.org/10.1002/adfm.202205115.

[31] D. Li, C. Sun, T. Yan, J. Yuan, Y. Zou, *ACS Cent. Sci.* **2021**, *7*, 1787–1797, https://doi.org/10.1021/acscentsci.1c01250.

[32] J. Huang, T. Chen, L. Mei, M. Wang, Y. Zhu, J. Cui, Y. Ouyang, Y. Pan, Z. Bi, W. Ma, Z. Ma, H. Zhu, C. Zhang, X.-K. Chen, H. Chen, L. Zuo, *Nat. Commun.* **2024**, *15*, 3287. https://doi.org/10.1038/s41467-024-47707-5.

[33] H. Hu, J. Ge, Z. Chen, W. Song, L. Xie, Z. Ge, *Adv. Energy Mater.* **2024**, *14*, 2304242. https://doi.org/10.1002/aenm.202304242.

[34] T. Li, K. Wang, G. Cai, Y. Li, H. Liu, Y. Jia, Z. Zhang, X. Lu, Y. Yang, Y. Lin, *JACS Au* **2021** *1*, 1733–1742, https://doi.org/10.1021/jacsau.1c00306.

[35] W. Gao, H. Fu, Y. Li, F. Lin, R. Sun, Z. Wu, X. Wu, C. Zhong, J. Min, J. Luo, H. Y. Woo, Z. Zhu, A. K.-Y. Jen, *Adv. Energy Mater.* **2021**, *11*, 2003177, https://doi.org/10.1002/aenm.202003177.

[36] Z. Chen, Y. Xiao, H. Yao, J. Ren, T. Zhang, J. Qiao, S. Zhu, R. Lin, X. Hao, J. Hou, *Adv. Mater.* **2024**, *36*, 2408858, https://doi.org/10.1002/adma.202408858.

[37] S. Feng, C. Zhang, Y. Liu, Z. Bi, Z. Zhang, X. Xu, W. Ma, Z. Bo, *Adv. Mater.* **2017**, *29*, 1703527, https://doi.org/10.1002/adma.201703527.

[38] J. Cao, T. Shan, J.-K. Wang, Y.-X. Xu, X. Ren, H. Zhong, *Dyes Pigm.* **2019**, *165*, 354–360, https://doi.org/10.1016/j.dyepig.2019.02.046.

[39] N. Minoi, F. Ishiwari, K. Murotani, R. Nishikubo, T. Fukushima, A. Saeki, *ACS Appl. Mater. Interfaces* **2023**, *15*, 6708–6715, https://doi.org/10.1021/acsami.2c18446.

[40] N. Minoi, F. Ishiwari, T. Omine, K. Murotani, R. Nishikubo, A. Saeki, *Sustainable Energy Fuels* **2024**, *8*, 4453–4460, https://doi.org/10.1039/D4SE01096E.

[41] T. Omine, F. Ishiwari, T. Won, N. Aizawa, Y. Takeda, Y. Yakiyama, T. Mori, K.-I. N. T. Hirose, A. Saeki, *ChemRxiv* **2024**, preprint10.26434/chemrxiv-2024-m8drx

[42] F. Ishiwari, T. Omine, A. Saeki, K. Munro, M. Buck, M. Zharnikov, *Chem. - Eur. J.* **2025**, *31*, e202404750, https://doi.org/10.1002/chem.202404750.

[43] S. Li, F. Ishiwari, S. Zorn, K. Murotani, M. Pylnev, K. Taniguchi, A. Saeki, *Chem. Commun.* **2024**,*60*, 10870–10873, https://doi.org/10.1039/D4CC03292F.

[44] L. Hong, H. Yao, R. Yu, Y. Xu, B. Gao, Z. Ge, J. Hou, *ACS Appl. Mater. Interfaces* **2019**, *11*, 29124–29131, https://doi.org/10.1021/acsami.9b10243.

[45] X. Liu, B. M. Xie, C. H. Duan, Z. J. Wang, B. B. Fan, K. Zhang, B. J. Lin, F. J. M. Colberts, W. Ma, R. A. J. Janssen, F. Huang, Y. Cao, *J. Mater. Chem. A* **2018**, *6*, 395–403, https://doi.org/10.1039/C7TA10136H.

[46] S. Torabi, F. Jahani, I. Van Severen, C. Kanimozhi, S. Patil, R. W. A. Havenith, R. C. Chiechi, L. Lutsen, D. J. M. Vanderzande, T. J. Cleij, J. C. Hummelen, L. J. A. Koster, *Adv. Funct. Mater.* **2015**, *25*, 150–157, https://doi.org/10.1002/adfm.201402244.

[47] P. Pananusorn, H. Sotome, H. Uratani, F. Ishiwari, K. Phomphrai, A. Saeki, *J. Chem. Phys.* **2024**, *161*, 184710, https://doi.org/10.1063/5.0227785.

[48] M. Saladina, P. Simón Marqués, A. Markina, S. Karuthedath, C. Wöpke, C. Göhler, Y. Chen, M. Allain, P. Blanchard, C. Cabanetos, D. Andrienko, F. Laquai, J. Gorenflot, C. Deibel, *Adv. Funct. Mater.* **2021**, *31*, 2007479, https://doi.org/10.1002/adfm.202007479.

[49] G. Albano, G. Pescitelli, L. D. Bari, *Chem. Rev.* **2020**, *120*, 10145–10243, https://doi.org/10.1021/acs.chemrev.0c00195.

[50] B. P. Bloom, Y. Paltiel, R. Naaman, D. H. Waldeck, *Chem. Rev.* **2024**, *124*, 1950–1991, https://doi.org/10.1021/acs.chemrev.3c00661.

[51] R. Nakajima, D. Hirobe, G. Kawaguchi, Y. Nabei, T. Sato, T. Narushima, H. Okamoto, H. M. Yamamoto, *Nature* **2023**, *613*, 479–484, https://doi.org/10.1038/s41586-022-05589-x.

[52] Y. Li, Z. Zhang, T. Li, Y. Liang, W. Si, Y. Lin, *Angew. Chem., Int. Ed.* **2023**, *62*, e202307466, https://doi.org/10.1002/anie.202307466.

[53] A. Saeki, *Polym. J.* **2020**, *52*, 1307–1321, https://doi.org/10.1038/s41428-020-00399-2.

[54] C. Nishikawa, R. Nishikubo, F. Ishiwari, A. Saeki, *JACS Au.* **2023**, *3*, 3194–3203, https://doi.org/10.1021/jacsau.3c00519.

[55] T. Song, E. Anderson, M. W.-Y. Tu, K. Seyler, T. Taniguchi, K. Watanabe, M. A. McGuire, X. Li, T. Cao, D. Xiao, W. Yao, X. Xu, *Sci. Adv.* **2021**, *7*, eabg8094, https://doi.org/10.1126/sciadv.abg8094.

Manuscript received: August 22, 2025
Revised manuscript received: October 15, 2025
Manuscript accepted: October 24, 2025
Version of record online: ■■, ■■